ACS APPLIED MATERIALS & INTERFACES

Research Article

Cite This: ACS Appl. Mater. Interfaces XXXX, XXX, XXX−XXX

www.acsami.org

Photocatalytic Nitrogen Oxide Removal Activity Improved Step-by-Step through Serial Multistep Cu Modifications

Liaoliao Zhao,[†] Guohui Dong,*[,†] Li Zhang,[‡] Yanfeng Lu,[§] and Yu Huang[§]

[†]School of Environmental Science and Engineering and [‡]School of Material Science and Engineering, Shaanxi University of Science and Technology, Xi'an 710021, China

[§]Key Laboratory of Aerosol Chemistry and Physics, Institute of Earth Environment, Chinese Academy of Sciences, Xi'an 710061, China

Supporting Information

ABSTRACT: Previous research has evidenced the insufficient efficiency in a one-step modified photocatalyst for NO removal. In this article, a serial multistep modification was explored to improve the NO removal activity of g-C_3N_4. In the experiment, a g-C_3N_4 photocatalyst has been successfully modified by Cu elements three times on one continuous process. Meanwhile, results showed that the serial multistep modifications could improve NO removal activity by g-C_3N_4 step by step. The main active species in the g-C_3N_4 system were h^+ and $^{\bullet}O_2^-$ but they were h^+ and $^{\bullet}OH$ in the three-modified g-C_3N_4 systems. Moreover, different mechanisms of activity improvement caused by the modified Cu in the serial-modified samples were identified. In the first modified sample, Cu^{2+} can decompose H_2O_2 molecules into $^{\bullet}OH$ via a Fenton-like reaction. In the second modified sample, the H_2O_2 molecule is activated by Cu^0 and decomposed into $^{\bullet}OH$ by the generated photoelectrons. After the third modification, the synergistic effects of the N vacancy and Cu^0 were identified, which significantly enhanced the photocatalytic NO removal activity of g-C_3N_4. This study proposed that the serial multistep modification can be a promising method to improve the NO removal activity of g-C_3N_4 stage-by-stage.

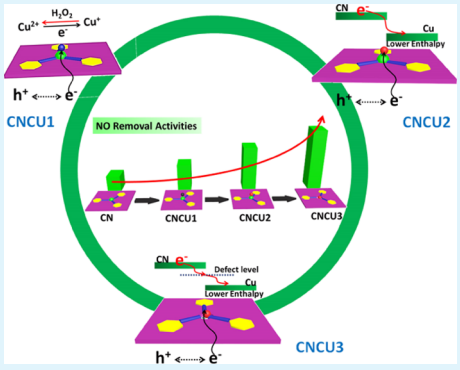

KEYWORDS: *surface modification, Cu modification, phocatalysis, NO removal, g-C_3N_4*

1. INTRODUCTION

Nitrogen oxide (NO_x) from the combustion of fossil fuels is one of the major air pollutants in cities.[1,2] Although NO_x consists of different types, such as N_2O, NO, NO_2, N_2O_3, and N_2O_5, 95% of NO_x pollutants are NO. The toxicity of NO can gradually deteriorate people's lungs and further trigger respiratory system diseases such as lung cancer, emphysema, and asthma.[3,4] Various technologies and methods (including wet absorption, selective catalytic reduction, selective catalytic oxidation, and photocatalysis.) have been developed for NO removal. Among these, photocatalytic technologies are one of the most promising methods for low concentration NO (ppb level) removal because of its moderate reaction conditions, convenient operation processes, and the abundance of solar energy.[5,6] In a typical photocatalytic technology, photocatalysts are the key roles because it produces large amounts of active species for NO removal. To date, many kinds of photocatalysts have been proven to be efficient in removing NO under light irradiation.[7−10] However, the removal efficiency of these photocatalysts cannot meet our expectations so far. For example, some photocatalysts are restricted to low visible light absorption abilities and low separation effects by photogenerated carriers, while other photocatalysts are plagued by photocorrosion.[11,12]

Therefore, many modification methods have been developed to improve the NO removal activity of these photocatalysts.[13−16] However, in previous studies, almost all photocatalysts were revised by one-step modifications with a single method. Further modifications that can produce faster, higher, and stronger NO removal activities are untapped. Also, it is suspected that a modification method with modified materials will produce more effective activity than the same modification method applied on the same material without modification. Moreover, multistep modification using different methods could potentially produce some synergistic effects to further improve the NO removal activity of the photocatalyst.

Previous literatures have reported that the multistep modification is an effective method to realize specific modification or performance such as light-controllable wettability properties.[17,18] However, to the best of our knowledge, there is no report regarding using multistep modification methods to improve the NO removal activity of a specific photocatalyst. Therefore, it is necessary to explore the multistep modification of photocatalysts for NO removal.

Received: January 3, 2019
Accepted: February 20, 2019
Published: February 20, 2019

DOI: 10.1021/acsami.9b00111
ACS Appl. Mater. Interfaces XXXX, XXX, XXX−XXX

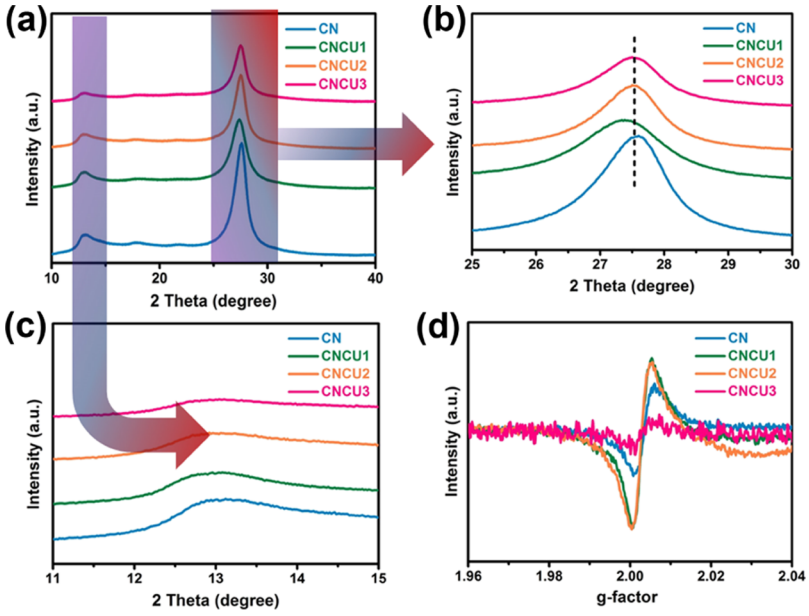

Figure 1. XRD patterns (a), partial enlargement of XRD patterns (b,c), and EPR spectra (d) of CN, CNCU1, CNCU2, and CNCU3 samples.

In this work, layered graphitic carbon nitride (g-C_3N_4) was chosen as the modification photocatalyst based on the following reasons: (1) among numerous photocatalysts, g-C_3N_4 is a metal-free polymer semiconductor that is convenient for synthesis and continuous modification;[19−21] (2) the modification of g-C_3N_4 is worthwhile because it is a promising photocatalyst in the NO removal field because of its chemical stability and low cost;[22−25] and (3) the band gap (ca. 2.7 eV) of pure g-C_3N_4 can tolerate a modest decrease or increase in the band gap.[26] Meanwhile, Cu has been considered as promising catalysts because of its nontoxicity, environmentally friendly, and natural abundance. Therefore, the divalent copper ion (Cu^{2+}) was chosen as the dopant for the first-step modification of g-C_3N_4. Cu^{2+} can form a coordination complex with ligands such as amidogen, which always distributes on the surface and the edge of g-C_3N_4. Based on the first-step modification, the second-step modification can be performed by reducing the doped Cu^{2+} to Cu^0. We will further investigate if the Cu^0 obtained from coordinated Cu^{2+} may lead to higher activity than free Cu^{2+}. Based on second-step modification, the g-C_3N_4 structure around Cu^0 is more likely to decompose under calcination conditions because of the "heat island effect" (the temperature of one area is higher than nearby areas.) of metal nanoparticles. Therefore, a third-step modification could be launched by calcining the second-step-modified sample under an inert atmosphere. After calcination, defects may appear around Cu^0 and produce the synergistic effects associated with Cu^0. This synergistic effect may improve the NO removal of g-C_3N_4 significantly.

In this study, g-C_3N_4 modified by Cu^{2+} ions have been synthesized by a continuous three-step process. Throughout the modification process, each step modification was based on the previous one. After the NO removal experiments, the photocatalyst activity was observed to be a reverse order as follows: third step-modified g-C_3N_4 > second step-modified g-C_3N_4 > first step-modified g-C_3N_4 > g-C_3N_4. More importantly, the activity of the second step-modified g-C_3N_4 was much higher than its counterpart, which was generated from the direct reduction of free Cu^{2+}. Meanwhile, the activity of the third step-modified g-C_3N_4 was also much higher than the sample, which was generated from direct co-calcination. Thus, a series of experiments were designed to reveal the mechanisms of improved activity in each step-modified sample.

2. EXPERIMENTAL SECTIONS

2.1. Synthesis of Samples. A g-C_3N_4 was synthesized by solid-phase synthesis. In a typical process, 3 g of melamine was placed in an alumina crucible (30 mL) with a cover. Then, the crucible was heated to 520 °C at the rate of 20 °C/min. After remaining at this temperature for 4 h, a yellow product was formed in the crucible. This was then ground into a powder and collected in a sample tube. This sample was denoted as CN.

To fabricate the Cu^{2+} coordination-modified g-C_3N_4 samples, 1 g of the CN sample was dispersed into 100 mL of distilled water. Then, an appropriate amount of $CuCl_2$ was added to the above suspension solution under stirring. Because the surface of g-C_3N_4 is electronegative, the positive electricity of Cu^{2+} can be neutralized by the electronegativity of the surface of g-C_3N_4 (Figure S1, in the Supporting Information). Additionally, the chloride ion cannot remain in the g-C_3N_4 structure because the negative charges repel each other. During this process, the weight ratios of Cu^{2+}/g-C_3N_4 were controlled as 0.1, 0.3, 0.5, and 0.6 wt %. Subsequently, the above mixtures were stirred for 4 h under dark conditions. After stirring, the suspensions underwent centrifugation, washing, and drying (60 °C) processes. Then, the Cu^{2+}-modified g-C_3N_4 samples were produced. According to the activity detection (Figure S2), the optimal weight ratios of Cu^{2+}/g-C_3N_4 was 0.3 wt %. Therefore, the sample with the weight ratios of 0.3 wt % was denoted as CNCU1 (the real loading content of Cu^{2+} measured by inductively coupled plasma atomic emission spectroscopy was 0.091 wt % in the CNCU1 sample).

The Cu^0-deposited g-C_3N_4 samples were prepared from Cu^{2+} coordination-modified g-C_3N_4 samples using the photodeposition method. First, 1 g of the prepared CNCU1 sample was dispersed in 100 mL distilled water that contains 4 mL methanol. Then, this suspension was illuminated by full spectrum light from a xenon lamp for 4 h under continuous stirring. During the photoreduction process, argon gas was continuously bubbled into and above the suspension to eliminate the dissolved oxygen. After photoreduction, the above suspensions underwent centrifugation, washing, and drying (60 °C) processes. Finally, the Cu^0-deposited g-C_3N_4 samples were produced and denoted as CNCU2. The synthesis of its counterpart (Cu^0/g-

DOI: 10.1021/acsami.9b00111
ACS Appl. Mater. Interfaces XXXX, XXX, XXX−XXX

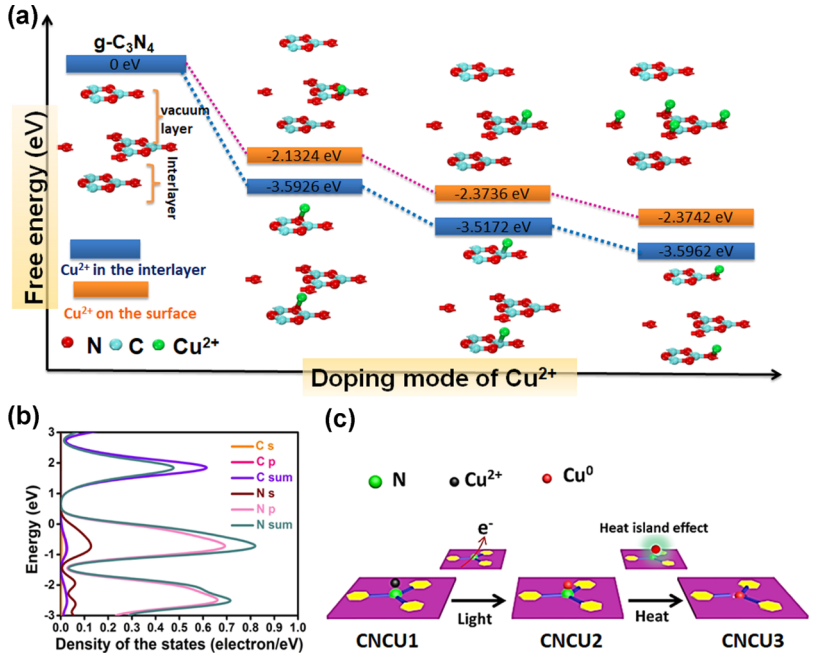

Figure 2. Free energy of several possible modes of Cu^{2+} doping CN (a); DOS of the CN (b); schematic illustration of the formation process of CNCU1, CNCU2, and CNCU3 samples (c).

C_3N_4) that was generated from the direct reduction of free Cu^{2+} can be found in the Supporting Information.

The prepared CNCU2 samples were placed into an aluminum boat. This boat was then placed in a tube furnace and heated at 520 °C for 2 h under argon gas protection. After the calcination process, the furnace with the sample was cooled to room temperature. Then, dark yellow samples were obtained from the alumina boat. The dark yellow samples were denoted as CNCU3. The synthesis of its counterpart (Cu_v/g-C_3N_4) that was generated from the direct cocalcination can be found in the Supporting Information.

2.2. Photocatalytic Experiment. To investigate the photocatalytic activity of the samples, photocatalytic NO removal experiments were performed in a continuous flow column-form reactor (R = 5 cm, H = 10 cm). The reactor was made from Pyrex glass with a quartz skylight. A prepared sample dish (R = 3 cm; H = 1.5 cm; weight = 22.2 g) was placed in the middle of the reactor. A 300 W Xe lamp with a 420 nm cutoff filter was chosen as the visible light source. It was vertically placed above the quartz skylight in the reactor (the distance between the light and the catalyst is 10 cm). Meanwhile, the air stream contained 600 ppb of NO continually passing through the reactor with the flow rate of 1 L/min. The change in the NO concentration was continuously measured using a NO_x analyzer (Thermo Scientific, 42i). The photos and diagram of the reaction setup can be found in the Supporting Information (Figure S3).

Other experiments including theoretical calculation, photoelectrochemical (PEC) experiments, determination of hydroxyl radical and hydrogen peroxide, the trapping experiment, and characterization can be found in the Supporting Information.

3. RESULTS AND DISCUSSION

3.1. Structure and Composition Analysis of Photocatalysts. X-ray diffraction (XRD) was employed to investigate the crystal structure of the resulting samples. As shown in Figure 1a, the XRD pattern of g-C_3N_4 displays two peaks at approximately 13.0° and 27.4°. The peak at 13.0° corresponds to the g-C_3N_4 (100) crystal plane, which was derived from the interplanar packing of triazine rings. Meanwhile, the peak at 27.4° corresponds to the stacking of the g-C_3N_4 (002) crystal plane.[27] When Cu^{2+} was doped in g-C_3N_4, the peak at 13.0° for CNCU1 was almost unchanged, indicating that the inner-plane structure of g-C_3N_4 was not damaged by Cu^{2+}. However, the peak at 27.4° for CNCU1 was shifted toward a lower 2θ value (Figure 1b), suggesting the distance of the (002) crystal layer became larger. This enlarged (002) crystal layer implied that Cu^{2+} may be introduced into the interlayer of g-C_3N_4 in the first-step modification. After the second modification, Cu^{2+} was reduced to Cu^0 by the photogenerated electrons. However, no corresponding Cu^0 peaks were observed from the XRD pattern of CNCU2, which could be associated with the low Cu^0 contents in CNCU2. Compared with CNCU1, the peak at 27.4° for CNCU2 shifted toward a higher 2θ value and returned to the value in g-C_3N_4. These phenomena indicated that the photoreduction could transfer the position of the Cu element from the interlayer to the surface. This point can be confirmed by the depth analyses of Cu auger electron spectroscopies (AES, Cu LMM) of (Figure S4). In CNCU1, the Cu^{2+} could still be detected in the inner parts about 20 nm depths. However, no Cu species could be detected in the inner parts of CNCU2. These results confirmed that the photoreduction could transfer the position of the Cu element from the interlayer to the surface. For CNCU3, the 2θ values of all the peaks remained unchanged compared to CNCU2. However, the intensity of the peak at 13.0° for CNCU3 was much weaker than for CNCU2 (Figure 1c), suggesting that the inner-plane structure of CNCU3 was destroyed during the calcination process because of the "heat island effect" (Cu nanoparticle as the "heat island"). Therefore, the inner-plane structure of CNCU3 was destroyed, which was confirmed by electron paramagnetic resonance (EPR) detection. As shown in Figure 1d, g-C_3N_4 had a strong EPR signal because of the conjugate electrons in the crystal plane structure of g-C_3N_4.[28] After the first and second modifications, the EPR signal increased because the delocalization of π-electrons increased.[29] However, after the third modification, the EPR signal of CNCU3 was unexpectedly lower than that of

DOI: 10.1021/acsami.9b00111
ACS Appl. Mater. Interfaces XXXX, XXX, XXX−XXX

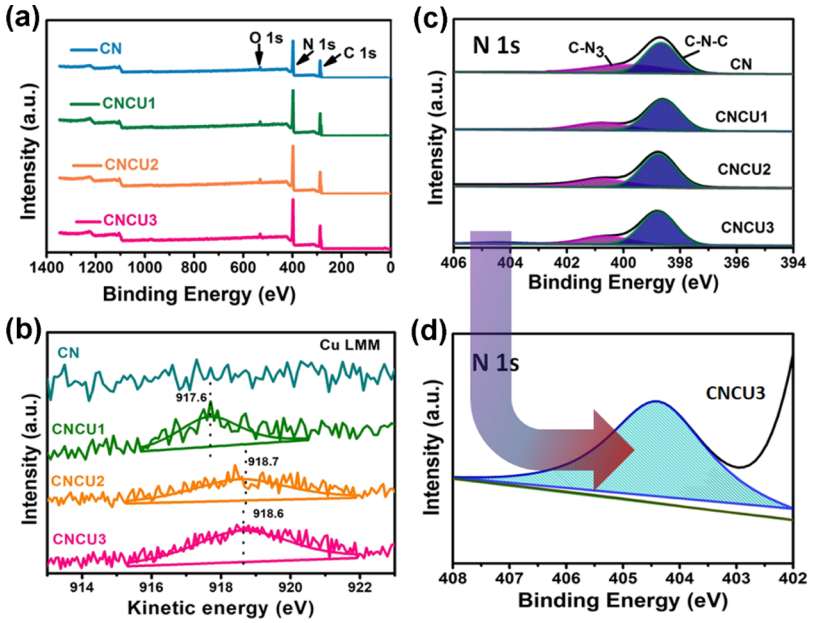

Figure 3. Survey spectra (a), Cu LMM spectra (b), N 1s spectra (c), and partial enlargement of N 1s spectra (d) of CN, CNCU1, CNCU2, and CNCU3 samples.

CN. This implied that the conjugate region decreased because of the formation of the defects in the structure of CNCU3.

The types of these defects in CNCU3 depended on the mode of Cu^{2+} doping. Density of functional theory (DFT) calculation was employed to investigate the energy of several possible modes of Cu^{2+} doping. First, we constructed a g-C_3N_4 crystal cell with a 15 Å vacuum layer (Figure S5a). In this crystal cell, it is assumed that Cu^{2+} can exist in the interlayer or on the surface of g-C_3N_4 (Figure S5b–g). Regardless of the interlayer or on the surface, Cu^{2+} has three possible binding objects, including C from the triazine ring, N from the triazine ring, and the bridging N. The doping energy ($E_{binding}$) was calculated with the following eq 1

$$E_{binding} = E_{(CN/Cu)} - E_{(CN)} - E_{(Cu)} \quad (1)$$

where $E_{(CN/Cu)}$, $E_{(CN)}$, and $E_{(Cu)}$ represent the energy of g-C_3N_4 binding with Cu, the energy of pure g-C_3N_4, and the energy of metal Cu, respectively. The calculation results (Figure 2a) showed that the energy of Cu^{2+} binding with the bridging N atom (on the surface: −2.3742 eV; in the interlayer: −3.5926 eV) was more negative than binding with C (on the surface: −2.3736 eV; in the interlayer: −3.5172 eV) and N (on the surface: −2.1342 eV; in the interlayer: −3.5962 eV) from the triazine ring. The more negative energy means a more stable system. Therefore, in the first-step modification, Cu^{2+} was mainly bound with the bridging N atom and existed in the interlayer, corresponding with the results from the XRD analysis. According to the density of the state (DOS) of pure g-C_3N_4, the conduction band for g-C_3N_4 is composed of an s orbital and a p orbital of the bridging N atom (Figure 2b). Therefore, Cu^{2+} could obtain photogenerated electrons from the bridging N and then be reduced to Cu^0. In other words, Cu^0 was covered on the bridging N after the second modification (Figure 2c); then, Cu^0 can induce the "heat island effect" and damage the bridging N to form the N vacancy during the calcination process (Figure 2c).

X-ray photoelectron spectroscopy (XPS) was performed to further investigate the elemental composition and valence state of different samples. Carbon, nitrogen, and oxygen could be found in the survey spectra of all the samples (Figure 3a). AES of Cu were used to study the chemical state of Cu in different samples. From Cu LMM spectra, the Cu LMM peak could be found from the three modified samples but not in that of CN, indicating that elemental Cu was introduced into the framework in the modified samples. However, the Cu LMM peak in CNCU1 was different from that in CNCU2 and CNCU3. In CNCU1, the Cu LMM peaked at approximately 917.6 eV because of Cu^{2+},[30] confirming the Cu^{2+} doping in the first modification. Moreover, there is no particle on the surface of CNCU1 according to the TEM image (Figure S6a). However, as shown in the energy-dispersive X-ray spectrometry images, Cu equally distribute on the surface of CNCU1 (Figure S6b,e). This information indicated that the nature of Cu^{2+} was cations. Meanwhile, the Cu LMM peaks in both CNCU2 and CNCU3 are at about 918.6 eV, which correspond to a zero-valent Cu.[31] This evidence supported that the valence of copper in the second and third modified samples was zero. According to Figure S6f,g, the size of the Cu particle in CNCU2 and CNCU3 is about 10 nm.

In addition to the Cu LMM spectra, the high-resolution N 1s XPS spectrum was also analyzed. As shown in Figure 3c, the peak of 398.4 eV could be attributed to the N atom from the triazine ring, while the peak at 400.7 eV arises from the bridging N atom (N−C_3) or amidogen. After the first modification, the peak of 400.7 eV shifted slightly by 0.2 eV to lower binding energies, suggesting the increase in the N atom electron density in N−C_3 or −NH_2. This phenomenon confirmed that the doped Cu^{2+} is bonded with the bridging N atom. The high-resolution N 1s XPS spectrum of CNCU2 is similar to that of CNCU1. For CNCU3, a new peak appeared at a high binding energy of 404 eV (Figure 3d), which was assigned to the N defect, confirming that the N vacancy formed in the third modification and coexisted with Cu^0. To confirm the formation of N vacancy in CNCU3, elemental analysis was used to study the contents of carbon and nitrogen in different samples. The content of carbon and nitrogen in the

DOI: 10.1021/acsami.9b00111
ACS Appl. Mater. Interfaces XXXX, XXX, XXX−XXX

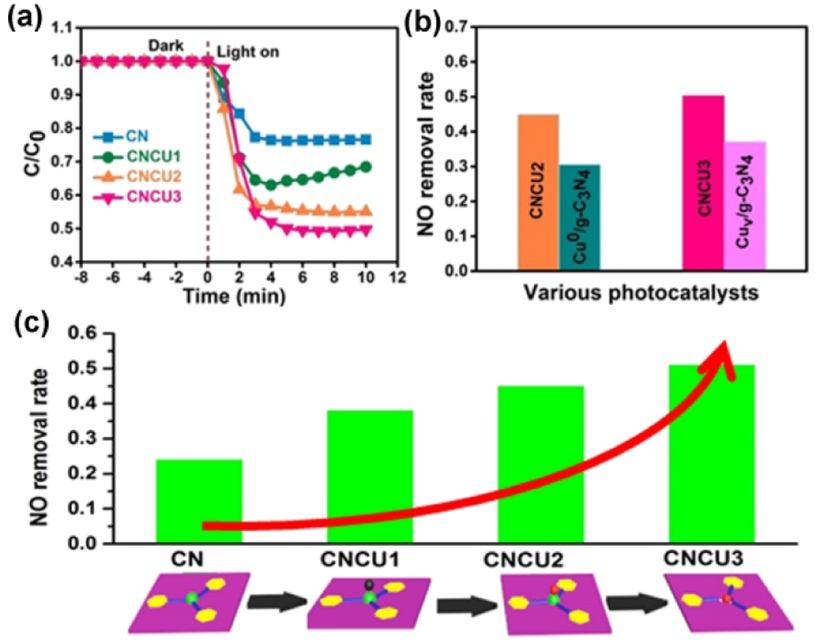

Figure 4. NO removal activities of CN, CNCU1, CNCU2, and CNCU3 samples (a); NO removal activity of $Cu^0/g\text{-}C_3N_4$, $Cu_v/g\text{-}C_3N_4$, CNCU1, and CNCU2 samples (b); effect of multistep modification on the NO removal activity of CN (c).

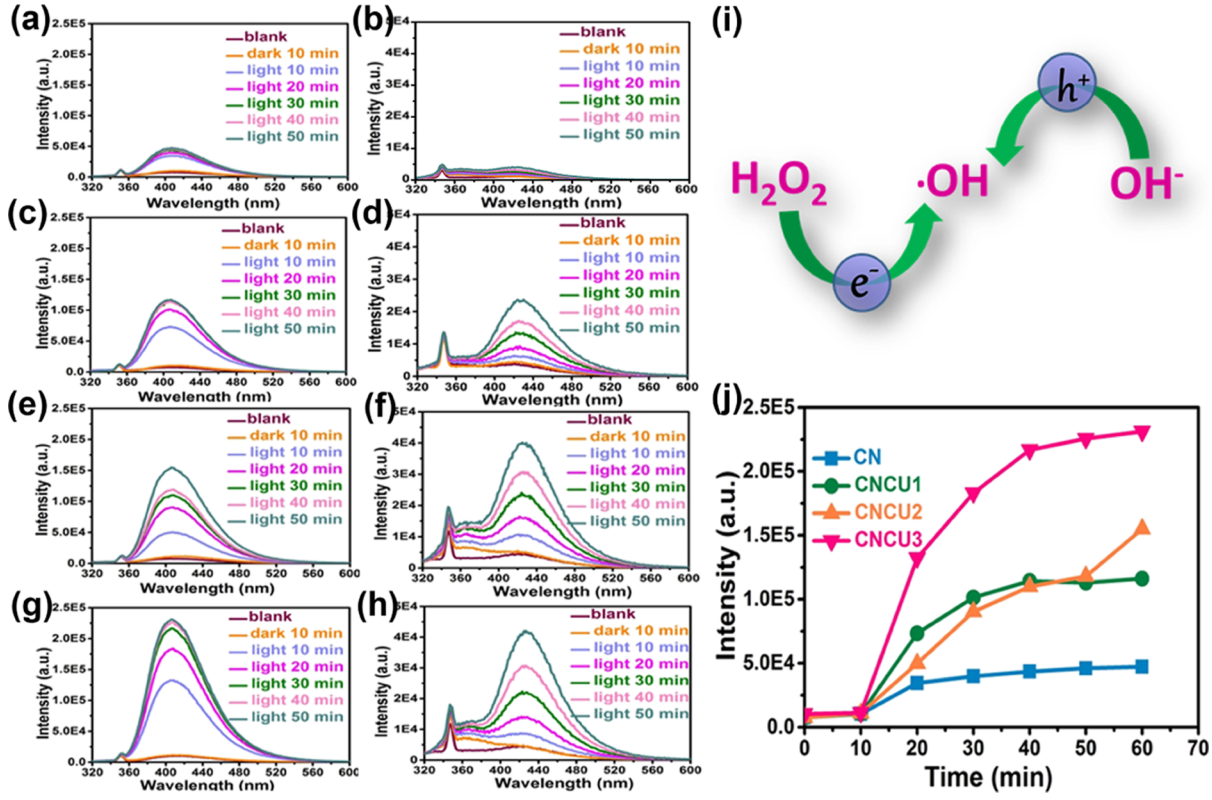

Figure 5. Generation of H_2O_2 (a) and $^{\bullet}OH$ (b) in the CN system; generation of H_2O_2 (c) and $^{\bullet}OH$ (d) in the CNCU1 system; the generation of the H_2O_2 (e) and $^{\bullet}OH$ (f) in CNCU2 system; the generation of the H_2O_2 (g) and $^{\bullet}OH$ (h) in the CNCU3 system; possible generation pathway of $^{\bullet}OH$ (i); generation curve of H_2O_2 on the CN, CNCU1, CNCU2, and CNCU3 samples (j).

$g\text{-}C_3N_4$ sample are 34.40 and 59.06%, respectively. Meanwhile, the content of carbon and nitrogen in the CNCU3 sample are 36.49 and 54.59%, respectively. The molar ratio of nitrogen to carbon (N/C) in $g\text{-}C_3N_4$ and CNCU3 are calculated as 1.5 and 1.3, respectively. This result confirmed that Cu^0 particles induced the formation of N vacancies in CNCU3 during the calcination process.

3.2. Activity Analysis of Photocatalysts. The photocatalytic activities of the as-prepared samples were evaluated based on the NO removal activity. As shown in Figure 4a, CNCU1 displayed a higher activity than pure $g\text{-}C_3N_4$. The NO

DOI: 10.1021/acsami.9b00111
ACS Appl. Mater. Interfaces XXXX, XXX, XXX−XXX

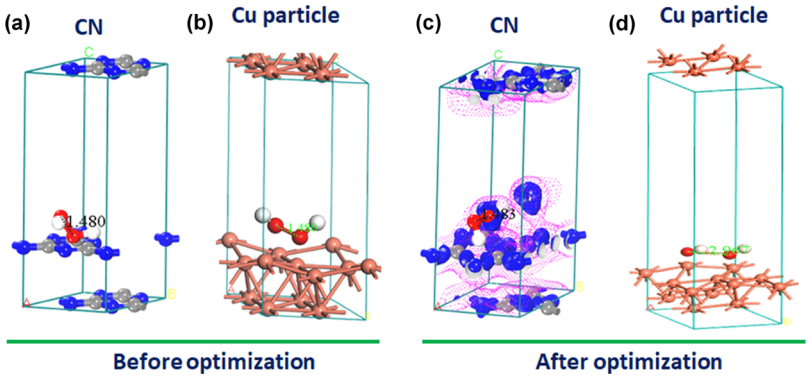

Figure 6. Before optimization of the CN crystal cell (a) and the metal Cu cell (b) with H_2O_2; after optimization of the CN crystal cell (c) and the metal Cu cell (d) with H_2O_2.

removal activity was increased by greater than 1.2 times when CNCU1 was transformed into CNCU2. Moreover, the NO removal rate of CNCU3 was further improved from 0.45 to 0.51 after calcination under an inert atmosphere. The activity of CNCU3 was 2.08 times (which is a huge boost in the continuous flow reactor), higher than that of CN. The above data implied that the further modification of the modified photocatalyst could possibly improve the photocatalytic activity of the photocatalyst (Figure 4c). This regularity could also be found in the H_2O_2 generation (Figure 5; as described in a later section) and rhodamine B (RhB) degradation (Figure S7; as described in the Supporting Information). To test whether a modification method used on a modified sample is superior to the method used on an unmodified sample, we synthesized the counterpart of CNCU2 and CNCU3 (Cu^0/g-C_3N_4 and Cu_v/g-C_3N_4). The NO removal activities of Cu^0/g-C_3N_4 and Cu_v/g-C_3N_4 (Figures 4b and S8a) were only six-tenths and seven-tenths of CNCU2 and CNCU3, respectively, suggesting that the modification method applied on a modified material will produce higher activity strengthening effects than that of the same method applied on the same material that has not undergone the modification (Figure 4c). The reasons will be analyzed later.

The concentration of NO_2 produced was also monitored. When the NO removal got to the equilibrium, the cumulative produced NO_2 in CN, CNCU1, CNCU2, and CNCU3 were 570, 480, 270, and 160 ppb, respectively (Figure S9a). Meanwhile, the generation of NO_3^- was confirmed by analyzing the washing solution of the used sample via ion chromatography. From the test results, the produced NO_3^- in the washing solution of used CN, CNCU1, CNCU2, and CNCU3 were 2.2, 4.6, 6.2, and 6.8 μg/L, respectively (Figure S9b). After the calculation, it is found that the formed NO_2 and NO_3^- could meet with the consumed NO, indicating no other products in the NO removal process. Based on above results, the NO_2 conversion rate of CN, CNCU1, CNCU2, and CNCU3 were 44, 25, 11, and 6%, respectively. Meanwhile, the NO_3^- conversion rate (NO to NO_3^-) of CN, CNCU1, CNCU2, and CNCU3 were 56, 75, 89, and 94%, respectively.

To test the stability of different samples for NO removal, photocatalytic NO removal cycles were performed with CN, CNCU1, CNCU2, and CNCU3 under fixed conditions. After five cycles, the NO removal capacities of all the samples remained constant (Figure S10), indicating that the photocatalytic activities of all the samples would be stable with repeated use.

3.3. Mechanism Analysis of Activity Enhancement.

To investigate the possible mechanisms of photocatalytic NO removal over different samples, active species scavenging experiments were performed. According to Figure S11a, the main contributors to NO removal on g-C_3N_4 are h^+ and $^\bullet O_2^-$. However, Figure S11b–d shows that the NO removal activities on three modified samples were mainly dependent on h^+ and $^\bullet$OH (the detailed analysis can be found in the Supporting Information). These phenomena suggested the modifications changed the NO removal pathway.

In the active species scavenging experiments, it can be concluded that NO was removed by holes and reactive oxygen species (ROSs such as $^\bullet O_2^-$ and $^\bullet$OH). Therefore, the role of photogenerated electrons was reasonably speculated to produce ROSs from the reduction of O_2. Previous reports showed that the photogenerated electrons from g-C_3N_4 can reduce O_2 to $^\bullet O_2^-$ (eq 2),[32] which may be further reduced to H_2O_2 (eq 3) and $^\bullet$OH (eq 4). To further investigate the mechanism of NO removal, a fluorophotometer was employed to detect H_2O_2 and $^\bullet$OH over different samples. Under darkness, no H_2O_2 or $^\bullet$OH signals can be detected in the g-C_3N_4, CNCU1, CNCU2, or CNCU3 systems. Under light illumination, the ROSs produced in different samples are different. In the g-C_3N_4 system, only H_2O_2 can be detected, and no $^\bullet$OH can be found (Figure 5a,b). The generated H_2O_2 gradually increases with the irradiation time. However, in the other three modified sample (CNCU1, CNCU2, and CNCU3) systems, both H_2O_2 and $^\bullet$OH can be detected (Figure 5c–h). According to a previous report,[33] $^\bullet$OH can be generated through an electron reduction pathway (eq 5) or hole oxidation pathway (eq 6) (Figure 5i). However, the valence band potential of g-C_3N_4 (1.4 V) is far smaller than the redox potential of $^\bullet$OH/OH^- (2.3 V), suggesting that holes are unable to oxidize OH^- to form $^\bullet$OH. Therefore, $^\bullet$OH in the three modified sample systems is generated from the decomposition of H_2O_2. This can be confirmed by the changing trends for H_2O_2 and $^\bullet$OH. The amount of H_2O_2 in the three systems increases and then tends to balance over time (Figure 5j), suggesting H_2O_2 can be decomposed in the three systems. With the balance of H_2O_2, the amount of $^\bullet$OH showed an increasing trend in the three modified sample systems. This indicated that $^\bullet$OH is generated from the decomposition of H_2O_2 in the three modified sample systems as the following equations shows

$$O_2 + e^- \rightarrow {}^\bullet O_2^- \quad (2)$$

DOI: 10.1021/acsami.9b00111
ACS Appl. Mater. Interfaces XXXX, XXX, XXX−XXX

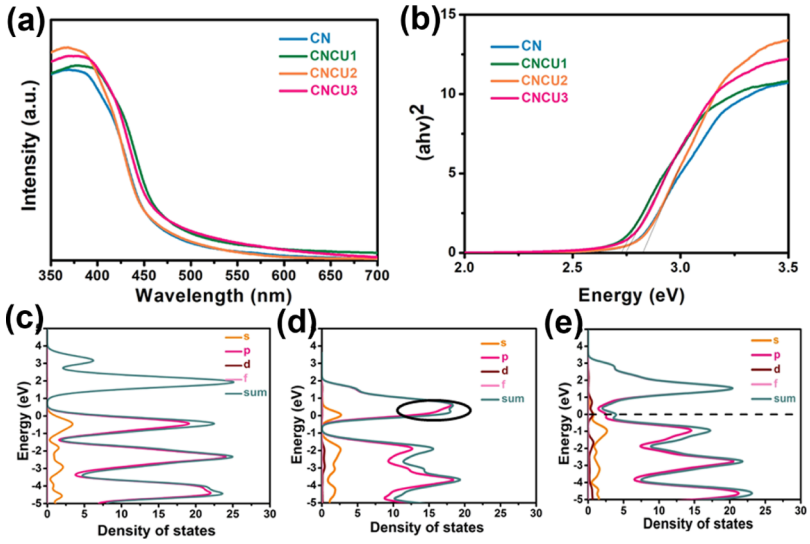

Figure 7. UV−vis diffuse reflectance spectra (a) and the band gaps (b) of the CN, CNCU1, CNCU2, and CNCU3 samples; calculated DOS of the CN (c), CNCU1 (d), and CNCU2 (e) samples.

$$^{\bullet}O_2^- + 2H^+ + e^- \rightarrow H_2O_2 \quad (3)$$

$$H_2O_2 + e^- \rightarrow {}^{\bullet}OH + OH^- \quad (4)$$

$$H_2O_2 + e^- \rightarrow {}^{\bullet}OH + OH^- \quad (5)$$

$$OH^- + h^+ \rightarrow {}^{\bullet}OH \quad (6)$$

Based on the changing trends for H_2O_2 and $^{\bullet}OH$ in the g-C_3N_4 system, it could be inferred that it is difficult for H_2O_2 to decompose on the g-C_3N_4 surface, which can be explained by the results from the DFT calculation. A g-C_3N_4 unit cell with a (001) vacuum layer was constructed to simulate the activation of H_2O_2 on the surface of g-C_3N_4. In this vacuum layer, an H_2O_2 monocular was located randomly (Figure 6a). Then, this unit cell with a vacuum layer and H_2O_2 monocular was optimized. After optimization, we noticed that the change in the H_2O_2 bond (O−O) length is very minor (Figure 6c), and it demonstrated that it is difficult to decompose H_2O_2 on the surface of g-C_3N_4.

Although it is difficult to decompose H_2O_2 on the surface of g-C_3N_4, it can be decomposed into $^{\bullet}OH$ on the surface of the CNCU1, CNCU2, and CNCU3 samples. According to previous reports, Cu^{2+} can decompose H_2O_2 into $^{\bullet}OH$ via a Fenton-like reaction (eqs 1 and 2).[34] Therefore, the detection of $^{\bullet}OH$ in the CNCU1 system was reasonable. Because Cu^0 does not induce the Fenton-like reaction, we speculate that H_2O_2 can be activated on the Cu^0 surface. In this case, H_2O_2 can be easily decomposed into $^{\bullet}OH$ by the generated electrons, which can be transferred from g-C_3N_4 to Cu^0. This can be proven by the previous DFT calculation. To simulate the activation of H_2O_2 on the surface of Cu^0, a Cu^0 unit cell with a (001) vacuum layer was constructed. In this vacuum layer, an H_2O_2 monocular was located randomly (Figure 6c). Then, the unit cell with the vacuum layer and H_2O_2 monocular was optimized. After optimization, the H_2O_2 bond (O−O) length had increased from 1.480 to 2.967 Å (Figure 6d), suggesting that H_2O_2 can be activated on the surface of Cu^0. The Fenton-like equations are shown in eqs 7 and 8

$$Cu^{2+} + H_2O_2 \rightarrow Cu^+ + {}^{\bullet}O_2^- + 2H^+ \quad (7)$$

$$Cu^+ + H_2O_2 \rightarrow Cu^{2+} + {}^{\bullet}OH + OH^- \quad (8)$$

To explore the mechanism for the activity improvement induced by the three modifications, the specific surface areas of the different samples were compared. This is because a bigger surface area contained more active sites, which is directly related to more photocatalytic activities. The specific surface areas of the different samples were evaluated by N_2 adsorption−desorption isotherms, as shown in Figure S8b. According to the IUPAC classification, all samples exhibited type V isotherms, indicating the presence of mesoporosity in the sample. Meanwhile, the surface areas of CN, CNCU1, CNCU2, and CNCU3 were 5.6, 5.7, 5.5, and 5.4 m^2/g, respectively. These similar surface area values suggested that the improved NO removal activity was not related to the specific surface area.

In addition to the specific surface area, the optical properties of the photocatalyst can also significantly affect the photoactivity of the photocatalyst. Therefore, UV−vis diffuse reflectance spectra were employed to investigate the light absorption abilities and band gaps of the different samples. As shown in Figure 7a, the absorption edge of CN is 450 nm. After the first modification, the absorption edge of CNCU1 had a red shift based on g-C_3N_4. However, this red shift disappeared when Cu^{2+} was transferring to Cu^0, indicating the red shift of the absorption edge after the first modification was caused by Cu^{2+} doping. Meanwhile, the second modification can recover the absorption edge from a long wavelength to that value of pristine g-C_3N_4, suggesting that Cu^0 does not affect the absorption edge of g-C_3N_4. More interestingly, the absorption edge of the third modified sample (CNCU3) showed the red shift once again. It is believed that this red shift was caused by the N vacancy generated in the third modification. The band gaps of CN, CNCU1, CNCU2, and CNCU3 are calculated to be 2.81, 2.73, 2.81, and 2.75 eV, respectively (Figure 7b). The red-shift absorption edge and the decrease in the band gap in the first and third modifications can be explained by the DOS calculations. Compared with the structure of CN, an impurity level appeared in the band gap of CNCU1 because of Cu 2p (Figure 7c), while a defect level appeared in the band gap of CNCU3 (Figure 7d). Because

DOI: 10.1021/acsami.9b00111
ACS Appl. Mater. Interfaces XXXX, XXX, XXX−XXX

impurity levels and defect levels can decrease the excitation energy of a semiconductor, the red-shift absorption edge and the decrease in the band gap in the first and third modifications can be explained.

After photoexcitation, the photogenerated electrons are likely to return to the valence band and recombine with the photogenerated holes. To investigate the separation rates of the photogenerated electrons and holes in the different samples, the photoluminescence (PL) spectra of different samples were studied (Figure 8). Based on the results of the

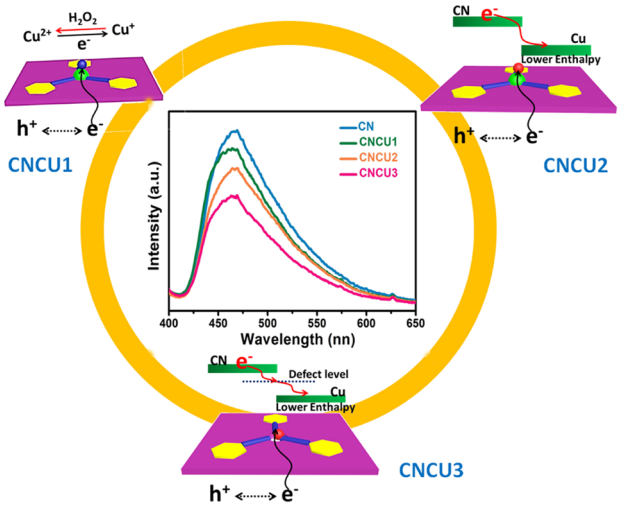

Figure 8. PL spectra of different samples and the mechanisms of lower PL intensities on CNCU1, CNCU2, and CNCU3.

light absorption and band gap, the following three hypotheses were proposed: (i) the emission peaks of CNCU1 and CNCU3 may shift to longer wavelengths than that of CN because of their lower band gaps; (ii) the PL intensity of CNCU1 may be stronger than that of CN because the lower band gap can induce more electron excitation; and (iii) the PL intensities of CNCU2 and CNCU3 may be shorter than that of CN because both Cu^0 and the N vacancy function to trap electrons. After the tests, hypothesis (i) and (iii) are supported by the testing results. However, the testing results opposed speculation (ii), implying that Cu^{2+} can capture photogenerated electrons or promote the transfer of photogenerated electrons.

To investigate the transfer efficiency of photogenerated carriers in different samples, photocurrent was measured (as shown in Figure 9a,b). It can be observed that the photocurrent density of CNCU1 is higher than that of CN, suggesting that Cu^{2+} can improve the transfer of electrons—not just capture the electrons. After the second modification, CNCU2 showed a higher current density than CNCU1, indicating that the promotion effect of Cu^0 was greater than that of Cu^{2+}. However, the photocurrent density of Cu^0/g-C_3N_4 was smaller than that of g-C_3N_4. This phenomenon confirmed that the Cu^0 generated in the second-step modification was more effective than that generated from direct reduction. The differences between CNCU2 (Cu^0-g-C_3N_4) and Cu^0/g-C_3N_4 may be related to the size of Cu^0 (Figure S12; the detailed analysis can be found in the Supporting Information). Cu^0/g-C_3N_4 and N_v/g-C_3N_4 also display a lower current density than CN in Figure 9b, which is consistent with our previous report that N vacancy can capture and confine the electrons.[35] Based on this result, it is speculated that the photocurrent density of CNCU3 will not exceed the photocurrent density of g-C_3N_4. However, the photocurrent density of CNCU3 is much larger than the photocurrent density of the other samples as shown in Figure 9a, revealing the synergistic effect exists between Cu^0 and the N vacancy (Figure 9c). Although the N vacancy is believed to capture and confine the electrons, it could actually transfer electrons to the embedded Cu^0. Then, Cu^0 could transfer electrons to adsorbed O_2 or H_2O_2. As a result, the carrier transfer efficiency in different samples is ranked as follows: CNCU3 > CNCU2 > CNCU1 > CN. This can be further proven by electrochemical impedance spectroscopy (EIS) as shown in Figure 9d.

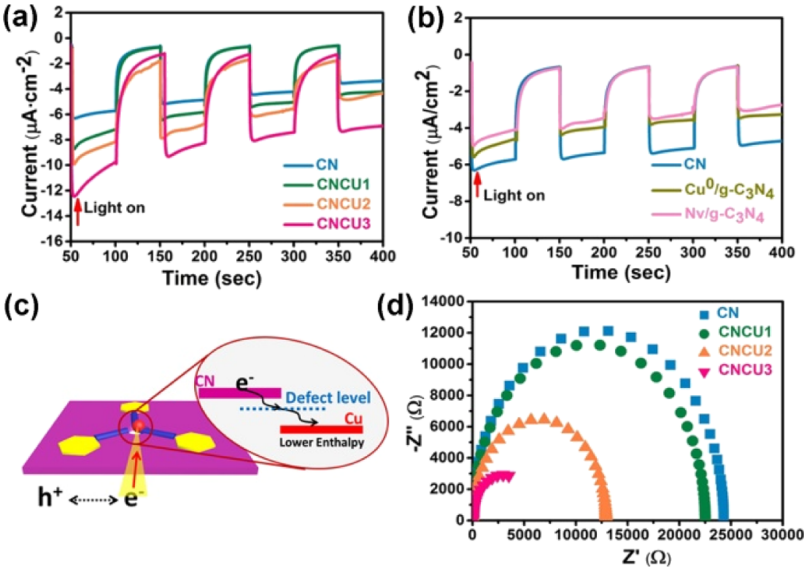

Figure 9. Photocurrents of the CN and multistep modified samples (a); photocurrents of CN, Cu^0/g-C_3N_4, and N_v-g-C_3N_4 (b); schematic illustration of the synergistic effect exists between Cu^0 and N vacancy (c); EIS of the CN, CNCU1, CNCU2, and CNCU3 samples (d).

DOI: 10.1021/acsami.9b00111
ACS Appl. Mater. Interfaces XXXX, XXX, XXX−XXX

4. CONCLUSIONS

In this article, a new method that successfully synthesized g-C_3N_4 samples using serial multistep modifications was introduced. This process began with the coordination of Cu^{2+} as the first-step modification (CNCU1). CNCU1 then underwent an in situ reduction to produce Cu^0-deposited g-C_3N_4 (CNCU2). Finally, CNCU2 was calcined under argon gas to construct the coexistence of an N vacancy and Cu^0 (CNCU3). In CNCU1, the Cu^{2+} ions can decompose H_2O_2 into $^{\bullet}OH$ through a Fenton-like reaction, thus improve the NO removal activity of g-C_3N_4. In the CNCU2, more $^{\bullet}OH$ can be produced because Cu^0 can activate H_2O_2. Therefore, the NO removal activity of g-C_3N_4 could be further improved. In the CNCU3 system, the synergistic effects between the N vacancy and Cu^0 could enable CNCU3 produce more $^{\bullet}OH$ than CNCU2. As a result, CNCU3 displayed the best NO removal activity. The results of the current study could illuminate future studies on serial multistep modification that can improve the NO removal activity of g-C_3N_4.

■ ASSOCIATED CONTENT

Supporting Information

The Supporting Information is available free of charge on the ACS Publications website at DOI: 10.1021/acsami.9b00111.

Preparation of Cu^0/g-C_3N_4 photocatalysts; preparation of Cu_v/g-C_3N_4 photocatalysts; first-principles DFT calculation methods; PEC experiment methods; fluorescence determination of hydroxyl radical and hydrogen peroxide; trapping experiment; characterization; detailed mechanism of NO removal; calculation process of N-balance; photocatalytic degradation of RhB; differences between CNCU2 and Cu^0/g-C_3N_4 related to the size of Cu^0; surface potential; optimization of the doping amount; photos of the reactor, lamp, and mass flow meters; Cu LMM depth analyses; CN crystal cell; TEM image; degradation of RhB in different sample systems; NO removal activity of CN; generation of NO_2 and NO_3; NO removal stability of different samples; trapping experiments in CN; and schematic illustration of the formation of Cu^0 in CNCU2 and Cu PDF)

■ AUTHOR INFORMATION

Corresponding Author

*E-mail: dongguohui@sust.edu.cn.

ORCID

Guohui Dong: 0000-0001-8498-3814

Yu Huang: 0000-0003-3334-4849

Notes

The authors declare no competing financial interest.

■ ACKNOWLEDGMENTS

Financial support by the National Nature Science Foundation of China (grant nos. 21603271 and 21876104) is gratefully appreciated. We gratefully acknowledge Dr. Jialing Ma (School of Psychology, University of Aberdeen) for language polishing.

■ REFERENCES

(1) Jiang, G.; Li, X.; Lan, M.; Shen, T.; Lv, X.; Dong, F.; Zhang, S. Monodisperse Bismuth Nanoparticles Decorated Graphitic Carbon Nitride: Enhanced Visible-Light-Response Photocatalytic NO Removal and Reaction Pathway. *Appl. Catal., B* **2017**, *205*, 532−540.

(2) Zhang, Q.; Huang, Y.; Xu, L.; Cao, J.-j.; Ho, W.; Lee, S. C. Visible-Light-Active Plasmonic Ag−$SrTiO_3$ Nanocomposites for the Degradation of NO in Air with High Selectivity. *ACS Appl. Mater. Interfaces* **2016**, *8*, 4165−4174.

(3) Chock, D. P.; Dunker, A. M.; Kumar, S.; Sloane, C. S. Effect of Nitrogen Oxides (NOx) Emission Rates on Smog Formation in the California South Coast Air Basin. *Environ. Sci. Technol.* **1981**, *15*, 933−939.

(4) Orme, I. M.; Robinson, R. T.; Cooper, A. M. The Balance between Protective and Pathogenic Immune Responses in the TB-Infected Lung. *Nat. Immunol.* **2015**, *16*, 57−63.

(5) Jin, S.; Dong, G.; Luo, J.; Ma, F.; Wang, C. Improved Photocatalytic NO Removal Activity of $SrTiO_3$ by Using $SrCO_3$ as A New Co-Catalyst. *Appl. Catal., B* **2018**, *227*, 24−34.

(6) Gao, Y.; Huang, Y.; Li, Y.; Zhang, Q.; Cao, J.-j.; Ho, W.; Lee, S. C. Plasmonic Bi/$ZnWO_4$ Microspheres with Improved Photocatalytic Activity on NO Removal under Visible Light. *ACS Sustainable Chem. Eng.* **2016**, *4*, 6912−6920.

(7) Ma, J.; Wang, C.; He, H. Enhanced Photocatalytic Oxidation of NO Over g-C_3N_4-TiO_2 Under UV and Visible Light. *Appl. Catal., B* **2016**, *184*, 28−34.

(8) Ai, Z.; Ho, W.; Lee, S. Efficient Visible Light Photocatalytic Removal of NO with BiOBr-Graphene Nanocomposites. *J. Phys. Chem. C* **2011**, *115*, 25330−25337.

(9) Ai, Z.; Zhang, L.; Lee, S. Efficient Visible Light Photocatalytic Oxidation of NO on Aerosol Flow-Synthesized Nanocrystalline $InVO_4$ Hollow Microspheres. *J. Phys. Chem. C* **2010**, *114*, 18594−18600.

(10) Li, H.; Shang, H.; Cao, X.; Yang, Z.; Ai, Z.; Zhang, L. Oxygen Vacancies Mediated Complete Visible Light NO Oxidation via Side-On Bridging Superoxide Radicals. *Environ. Sci. Technol.* **2018**, *52*, 8659−8665.

(11) Dong, F.; Zhao, Z.; Xiong, T.; Ni, Z.; Zhang, W.; Sun, Y.; Ho, W.-K. In Situ Construction of g-C_3N_4/g-C_3N_4 Metal-Free Heterojunction for Enhanced Visible-Light Photocatalysis. *ACS Appl. Mater. Interfaces* **2013**, *5*, 11392−11401.

(12) Xiao, S.; Pan, D.; Liang, R.; Dai, W.; Zhang, Q.; Zhang, G.; Su, C.; Li, H.; Chen, W. Bimetal MOF Derived Mesocrystal $ZnCo_2O_4$ on rGO with High Performance in Visible-Light Photocatalytic NO Oxidization. *Appl. Catal., B* **2018**, *236*, 304−313.

(13) Dong, G.; Yang, L.; Wang, F.; Zang, L.; Wang, C. Removal of Nitric Oxide through Visible Light Photocatalysis by g-C3N4 Modified with Perylene Imides. *ACS Catal.* **2016**, *6*, 6511−6519.

(14) Xiong, T.; Wen, M.; Dong, F.; Yu, J.; Han, L.; Lei, B.; Zhang, Y.; Tang, X.; Zang, Z. Three Dimensional Z-scheme $(BiO)_2CO_3$/MoS_2 With Enhanced Visible Light Photocatalytic NO Removal. *Appl. Catal., B* **2016**, *199*, 87−95.

(15) Hu, J.; Chen, D.; Li, N.; Xu, Q.; Li, H.; He, J.; Lu, J. Fabrication of G raphitic-C_3N_4 Quantum Dots/Graphene-$InVO_4$ Aerogel Hybrids With Enhanced Photocatalytic NO Removal Under Visible-Light Irradiation. *Appl. Catal., B* **2018**, *236*, 45−52.

(16) Lin, Y.-M.; Tseng, Y.-H.; Huang, J.-H.; Chao, C. C.; Chen, C.-C.; Wang, I. Photocatalytic Activity for Degradation of Nitrogen Oxides Over Visible Light Responsive Titania-Based Photocatalysts. *Environ. Sci. Technol.* **2006**, *40*, 1616−1621.

(17) Chng, S.; Moloney, M. G.; Wu, L. Y. L. Photochromic Materials by Postpolymerisation Surface Modification. *ACS Omega* **2018**, *3*, 15554−15565.

(18) Brockman, J. M.; Frutos, A. G.; Corn, R. M. A Multistep Chemical Modification Procedure To Create DNA Arrays on Gold Surfaces for the Study of Protein-DNA Interactions with Surface Plasmon Resonance Imaging. *J. Am. Chem. Soc.* **1999**, *121*, 8044−8051.

(19) Wang, X.; Maeda, K.; Thomas, A.; Takanabe, K.; Xin, G.; Carlsson, J. M.; Domen, K.; Antonietti, M. A Metal-Free Polymeric Photocatalyst for Hydrogen Production From Water Under Visible Light. *Nat. Mater.* **2009**, *8*, 76−80.

(20) Niu, P.; Yin, L.-C.; Yang, Y.-Q.; Liu, G.; Cheng, H.-M. Increasing the Visible Light Absorption of Graphitic Carbon Nitride

DOI: 10.1021/acsami.9b00111
ACS Appl. Mater. Interfaces XXXX, XXX, XXX−XXX

(Melon) Photocatalysts by Homogeneous Self-Modification with Nitrogen Vacancies. *Adv. Mater.* **2014**, *26*, 8046−8052.
(21) Yang, L.; Dong, G.; Jacobs, D. L.; Wang, Y.; Zang, L.; Wang, C. Two-Channel Photocatalytic Production of H_2O_2 over g-C_3N_4 Nanosheets Modified with Perylene Imides. *J. Catal.* **2017**, *352*, 274−281.
(22) Dong, F.; Wang, Z.; Li, Y.; Ho, W.-K.; Lee, S. C. Immobilization of Polymeric g-C3N4 on Structured Ceramic Foam for Efficient Visible Light Photocatalytic Air Purification with Real Indoor Illumination. *Environ. Sci. Technol.* **2014**, *48*, 10345−10353.
(23) Li, J.; Zhang, Z.; Cui, W.; Wang, H.; Cen, W.; Johnson, G.; Jiang, G.; Zhang, S.; Dong, F. The Spatially Oriented Charge Flow and Photocatalysis Mechanism on Internal Van der Waals Heterostructures Enhanced g-C_3N_4. *ACS Catal.* **2018**, *8*, 8376−8385.
(24) Cui, W.; Li, J.; Sun, Y.; Wang, H.; Jiang, G.; Lee, S. C.; Dong, F. Enhancing ROS Generation and Suppressing Toxic Intermediate Production Inphotocatalytic NO Oxidation on O/Ba Co-Functionalized Amorphous Carbon Nitride. *Appl. Catal., B* **2018**, *237*, 938−946.
(25) Li, J.; Dong, X. A.; Sun, Y.; Jiang, G.; Chu, Y.; Lee, S. C.; Dong, F. Tailoring The Rate-Determining Step In Photocatalysis Via Localized Excess Electrons For Efficient And Safe Air Cleaning. *Appl. Catal., B* **2018**, *239*, 187−195.
(26) Qin, J.; Wang, S.; Ren, H.; Hou, Y.; Wang, X. Photocatalytic Reduction of CO_2 By Graphitic Carbon Nitride Polymers Derived From Urea And Barbituric Acid. *Appl. Catal., B* **2015**, *179*, 1−8.
(27) Ho, W.; Zhang, Z.; Lin, W.; Huang, S.; Zhang, X.; Wang, X.; Huang, Y. Copolymerization With 2,4,6-Triaminopyrimidine For The Rolling-up The Layer Structure, Tunable Electronic Properties, And Photocatalysis of g-C_3N_4. *ACS Appl. Mater. Interfaces* **2015**, *7*, 5497−5505.
(28) Zhang, J.; Zhang, G.; Chen, X.; Lin, S.; Möhlmann, L.; Dołęga, G.; Lipner, G.; Antonietti, M.; Blechert, S.; Wang, X. Co-Monomer Control of Carbon Nitride Semiconductors To Optimize Hydrogen Evolution With Visible Light. *Angew. Chem., Int. Ed.* **2012**, *51*, 3183−3187.
(29) Liu, Q.; Chen, T. X.; Guo, Y. R.; Zhang, Z. G.; Fang, X. M. Grafting Fe(III) Species on Carbon Nanodots/Fe-Doped g-C_3N_4 Via Interfacial Charge Transfer Effect For Highly Improved Photocatalytic Performance. *Appl. Catal., B* **2017**, *205*, 173−181.
(30) Martin, L.; Martinez, H.; Poinot, D.; Pecquenard, B.; Le Cras, F. Comprehensive X-ray Photoelectron Spectroscopy Study of The Conversion Reaction Mechanism of CuO In Lithiated Thin Film Electrodes. *J. Phys. Chem. C* **2013**, *117*, 4421−4430.
(31) Liu, B.-H.; Groot, I. M. N.; Pan, Q.; Shaikhutdinov, S.; Freund, H.-J. Ultrathin Zn And ZnO Films on Cu(111) As Model Catalysts. *Appl. Catal., A* **2017**, *548*, 16−23.
(32) Dong, G.; Zhang, L. Synthesis and Enhanced Cr(VI) Photoreduction Property of Formate Anion Containing Graphitic Carbon Nitride. *J. Phys. Chem. C* **2013**, *117*, 4062−4068.
(33) Li, Y. X.; Ouyang, S. X.; Xu, H.; Ye, J. H. Constructing Solid−Gas-Interfacial Fenton Reaction Over Alkalinized-C_3N_4 Photocatalyst To Achieve Apparent Quantum Yield of 49% At 420 nm. *J. Am. Chem. Soc.* **2016**, *138*, 13289−13297.
(34) Lyu, L.; Yu, G.; Zhang, L.; Hu, C.; Sun, Y. 4-Phenoxyphenol-Functionalized Reduced Graphene Oxide Nanosheets: A Metal-Free Fenton-Like Catalyst For Pollutant Destruction. *Environ. Sci. Technol.* **2018**, *52*, 747−756.
(35) Dong, G.; Ho, W.; Wang, C. Selective Photocatalytic N_2 Fixation Dependent on g-C_3N_4 Induced By Nitrogen Vacancies. *J. Mater. Chem. A* **2015**, *3*, 23435−23441.

DOI: 10.1021/acsami.9b00111
ACS Appl. Mater. Interfaces XXXX, XXX, XXX−XXX